

Azimuthal and Radial Variation of Wind-Generated Surface Waves inside Tropical Cyclones

PAUL A. HWANG

Remote Sensing Division, Naval Research Laboratory, Washington, D.C.

EDWARD J. WALSH

NOAA/Earth System Research Laboratory, Physical Sciences Division, Boulder, Colorado

(Manuscript received 2 March 2016, in final form 23 May 2016)

ABSTRACT

For wind-generated waves, the wind-wave triplets (reference wind speed, significant wave height, and spectral peak wave period) are intimately connected through the fetch- or duration-limited wave growth functions. The full set of the triplets can be obtained knowing only one of the three, together with the input of fetch (duration) information using the pair of fetch-limited (duration limited) wave growth functions. The air-sea energy and momentum exchanges are functions of the wind-wave triplets, and they can be quantified with the wind-wave growth functions. Previous studies have shown that the wave development inside hurricanes follows essentially the same growth functions established for steady wind forcing conditions. This paper presents the analysis of wind-wave triplets collected inside Hurricane Bonnie 1998 at category 2 stage along 10 transects radiating from the hurricane center. A fetch model is formulated for any location inside the hurricane. Applying the fetch model to the 2D hurricane wind field, the detailed spatial distribution of the wave field and the associated energy and momentum exchanges inside the hurricane are investigated. For the case studied, the energy and momentum exchanges display two local maxima resulting from different weightings of wave age and wind speed. Referenced to the hurricane heading, the exchanges on the right half plane of the hurricane are much stronger than those on the left half plane. Integrated over the hurricane coverage area, the right-to-left ratio is about 3:1 for both energy and momentum exchanges. Computed exchange rates with and without considering wave properties differ significantly.

1. Introduction

Despite the complicated temporal and spatial distributions of the hurricane wind field, many analyses have shown that the generated surface waves follow the same similarity relationship as those produced by steady winds in fetch-limited conditions. For example, [Young \(1988\)](#) presents the analysis of a set of synthetic directional wave spectra simulated with model hurricane wind fields. Using the Joint North Sea Wave Project (JONSWAP) fetch-limited growth function of

significant wave height H_s ([Hasselmann et al. 1973](#)), he derives the effective fetch corresponding to the hurricane wind speed. The effective fetch is then used to compute the expected peak wave period T_p based on the JONSWAP fetch-limited wave period growth function. The wave periods derived from the numerical model and fetch-limited growth function are in very good agreement.

Subsequently, [Young \(1998, 2006\)](#) report the results from examining more than 20 yr of directional buoy recordings. Restricting the data to the condition that the buoy is within 8 times the radius of maximum wind speed from the hurricane center, he shows that the key parameters defining the directional wave spectra are not distinguishable between the hurricane waves and those observed in ideal steady wind fields. As a consequence of the wave spectral similarity, the wave growth function connecting the dimensionless wave variance and the dimensionless frequency $\eta_#(\omega_#)$ is the same for both sets

U.S. Naval Research Laboratory Publication Number JA/7260—16-0044.

Corresponding author address: Dr. Paul A. Hwang, Remote Sensing Division, Naval Research Laboratory, 4555 Overlook Avenue SW, Washington, DC 20375.
E-mail: paul.hwang@nrl.navy.mil

of wave fields generated by hurricane winds and steady winds. The dimensionless parameters are given by $\eta_{\#} = \eta_{\text{rms}}^2 g^2 U_{10}^{-4}$ and $\omega_{\#} = \omega_p U_{10} g^{-1}$, where the root-mean-square (rms) wave elevation η_{rms} is related to the significant wave height by $H_s = 4\eta_{\text{rms}}$, and the spectral peak angular frequency ω_p is $2\pi T_p^{-1}$, U_{10} is the reference neutral wind speed at 10-m elevation, and g is the gravitational acceleration. The similarity relation connects the three wind and wave variables (U_{10} , H_s , and T_p), which are referred to as the wind-wave triplets in this paper.

The nature of fetch- and duration-limited wave growth inside hurricanes is further elucidated with H_s and T_p measured by the airborne scanning radar altimeter (SRA) system and U_{10} from National Oceanic and Atmospheric Administration (NOAA) Hurricane Research Division (HRD) analysis in hurricane hunter missions. Using the 60 wave spectra of Hurricane Bonnie 1998 reported by Wright et al. (2001) and 12 wave spectra of Hurricane Ivan 2004 reported by Black et al. (2007), Hwang (2016) presents an analysis of the wave development inside hurricanes in terms of the wave age similarity, that is, $\eta_{\#}(\omega_{\#})$ discussed in the preceding paragraph as well as fetch- and duration-limited growth functions, that is, $\eta_{\#}(x_{\#})$, $\omega_{\#}(x_{\#})$, $\eta_{\#}(t_{\#})$, and $\omega_{\#}(t_{\#})$. In dimensionless form, the fetch x_f and duration t_d are given as $x_{\#} = x_f g U_{10}^{-2}$ and $t_{\#} = t_d g U_{10}^{-1}$, respectively. The 60 wave spectra of Hurricane Bonnie 1998 provide sufficient information for resolving the hurricane coverage area into three sectors (right, left, and back), as discussed in Black et al. (2007).

The 60 wave spectra reported by Wright et al. (2001) represent about a quarter of the full suite of the SRA wave measurements collected in that hurricane hunter mission. The full set contains 233 spectra along 10 transects radiating from the hurricane center. Here, we report the analysis of the full dataset that yields a much finer resolution in the azimuthal and radial variation of the surface wave development inside the hurricane (section 2).

The wave growth functions can be used to estimate the total (frequency integrated) rate of energy input or dissipation between air and water through the wave motion (e.g., Hwang and Sletten 2008; Hwang 2009). Similarly, the total rate of air-sea momentum exchange (momentum flux) can be parameterized with the wind-wave triplets (appendix). Section 3 describes the azimuthal and radial variation of the energy and momentum exchanges inside the hurricane computed with the wind-wave growth functions; the close correlation between momentum exchange and ocean surface wind stress is discussed. Section 4 presents a summary.

2. Surface wave development inside hurricane

a. SRA wave observation

The SRA wave measurements inside Hurricane Bonnie 1998 reported here span the time between 2030 UTC 24 August to 0144 UTC 25 August. Detailed discussions of the mission have been presented by Wright et al. (2001) and Moon et al. (2003); the information on the SRA operation and data analysis can be found in Walsh et al. (1985, 1989). Figures 1a to 1c show the wind-wave triplets (U_{10} , H_s , and T_p) plotted with respect to the position relative to the moving hurricane center. The flight tracks and the hurricane eye positions on Earth coordinates are given in Fig. 1 of Wright et al. (2001), which is reproduced in Fig. 1f for convenience. During the 4.7-h data acquisition time, the hurricane was moving in a steady north-northwest (NNW) direction. The advancing velocity estimated from the hurricane center positions is about 4.5 m s^{-1} , 13°N ; in this paper the azimuth angle increases counterclockwise (CCW). Using the hurricane heading as the reference, the dimensionless wave variance and peak frequency are plotted in Figs. 1d and 1e. In the remainder of this paper, the 2D hurricane data are plotted in the same format as Figs. 1d and 1e, with the hurricane heading pointing toward the top of the page, and subscript h is added to the Cartesian coordinates, that is, (x_h, y_h) , when referencing the hurricane heading. The data show the three-sector structure as discussed in Black et al. (2007) and Hwang (2016). For example, in dimensionless terms, the waves are youngest (large $\omega_{\#}$) in the back quarter of the hurricane, the wave age increases systematically (CCW in Northern Hemisphere), and the most mature waves are in the left-hand sector (Fig. 1e). Except for the region close to the eye, the dominant wave phase speed is less than the local wind speed, and they are classified as wind seas. During the period of data acquisition, the radius of the maximum wind speed r_m is about 74 km; see Table 1 of Moon et al. (2003). As will be shown later (in the discussion of Fig. 7), there is significant swell contribution within about 45 km from the hurricane center, and the waves near the eye region are mixed seas.

Figure 2 presents the wind and wave properties as functions of the radial distance r from the hurricane center with different colors and symbols to identify the data in four different quarters (Fig. 2f): green triangles, blue squares, black circles, and red diamonds for front (F), left (L), back (B), and right (R), respectively. In terms of the azimuth angle ϕ referenced to the hurricane heading, the ranges for the four quarters are $-45^\circ \sim 45^\circ$, $45^\circ \sim 135^\circ$, $135^\circ \sim 225^\circ$, and $225^\circ \sim 315^\circ$. For the U_{10} , H_s , and T_p plots (the top row), the data in the same quarter, but along different radial transects, can be recognized by

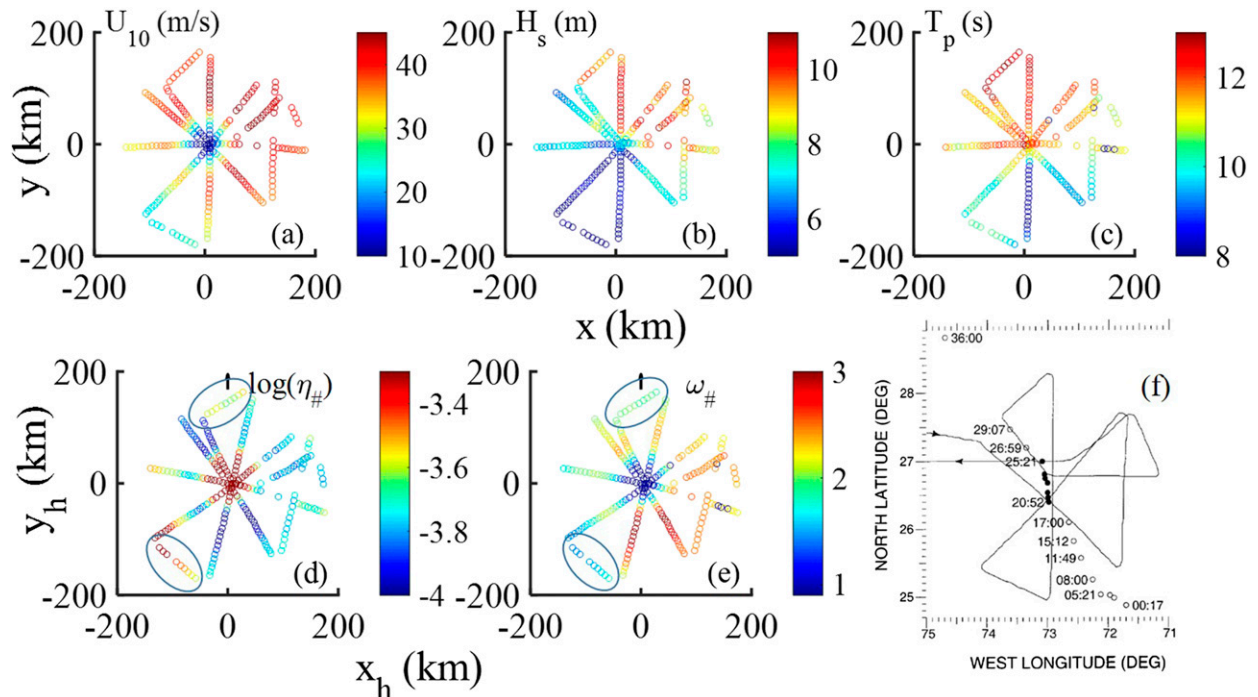


FIG. 1. (a) U_{10} , (b) H_s , (c) T_p , (d) $\log(\eta_{\#})$, and (e) $\omega_{\#}$ measured by the SRA inside Hurricane Bonnie 1998. (a), (b), and (c) are plotted in the east–west and north–south distances (x, y) with respect to the hurricane center in Earth coordinates. In (d) and (e), the coordinates are rotated such that the hurricane heading is toward the top of the page (x_h, y_h) are the left–right and front–back distances with respect to the hurricane center; data highlighted in ovals are discussed in more detail in the text. The data acquisition was completed in about 4.7 h, while the hurricane was moving. (f) Figure 1 of Wright et al. (2001) is reproduced, showing the longitude and latitude coordinates of the flight tracks with the positions of the hurricane centers superimposed. The time displayed in hour:minute UTC (hh:mm) is referenced to 24 Aug 1998; 24 h is added crossing over to 25 Aug 1998.

the identical symbol but with clear offset. When given in dimensionless form (Figs. 2d and 2e in the bottom row), the wind-wave parameters more or less sort into the four quarters, but the identity of an individual radial transect is still recognizable. Obviously, it is desirable to have a design describing the continuous azimuthal and radial variation of the surface wave field. One such design is presented in section 2b.

Figure 3 illustrates the same wind and wave data shown in Fig. 2 but given as a function of ϕ at several radial distances: $R_r = r/r_m = 0.25, 0.50, 0.65, 0.75, 1.10$, and 2.00 ($r_m = 74$ km). The range sorting bandwidth is $\Delta R_r = \pm 0.05$. Because the range band at $R_r = 1.00$ has wide gaps, the $R_r = 1.10$ band is shown for the wind and waves near the radius of maximum wind speed. The data gaps are usually associated with rainbands or aircraft maneuvering, causing deterioration of data quality.

For the wind field (Fig. 3a), the azimuthal variation can be sorted roughly into two groups: inward and outward of $R_r = 0.75$ ($r_m = 74$ km, $r = 56$ km). The outer group (Δ and o) shows smooth, quasi-sinusoidal variation with a broad region of high winds in the right-front sector

centered near $\phi = 315^\circ$. The inner group ($+$, x , and $*$) seems to develop higher harmonics, and the azimuthal distribution is more distorted with the peaks moving toward about $\phi = 220^\circ$ to 270° .

The azimuthal distributions of H_s (Fig. 3b) and T_p (Fig. 3c) are close to sinusoidal. The peak is near 0° for T_p , but more complicated for H_s ; for the outer group (Δ and o), the peak locations are similar to those of U_{10} , and for the inner group ($+$, x , and $*$), the peaks shift toward the hurricane heading (0°). The difference between the inner and outer groups separated by $R_r = 0.75$ are more localized; the magnitudes of H_s and T_p at different r show relatively small variations compared to U_{10} , with larger spread of the magnitude in the right quarter between 225° and 360° for H_s and in the back quarter between 135° and 225° for T_p .

The dimensionless wind-wave parameters of $\eta_{\#}$ (Fig. 3d) and $\omega_{\#}$ (Fig. 3e) also sort roughly into two groups separated by $R_r = 0.75$, mainly reflecting the U_{10} distribution. The waves are youngest (largest $\omega_{\#}$) near $r = r_m$ and become more mature toward both the inner and outer regions. The azimuthal distribution of $\eta_{\#}$ is approximately a mirror image of the $\omega_{\#}$ distribution as

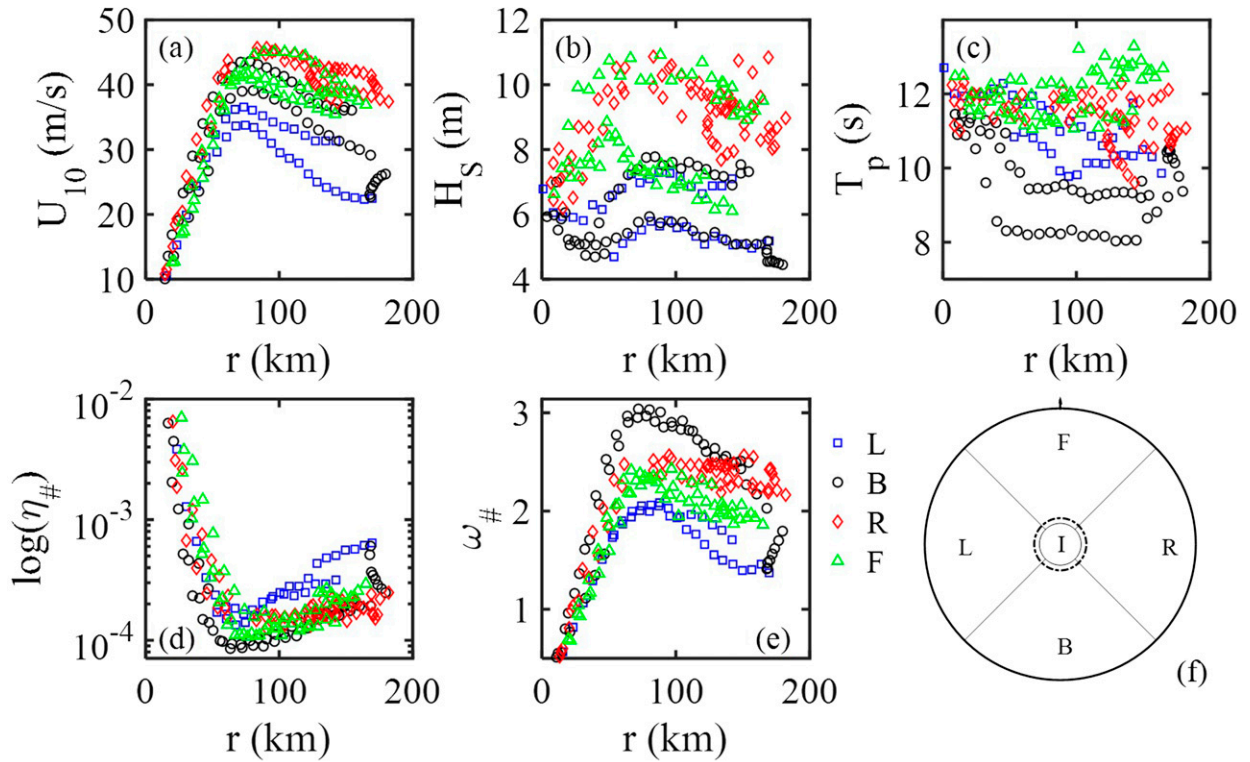


FIG. 2. As in Figs. 1a–e, but plotted with respect to the radial distance from the hurricane center; flight tracks in four different quarters (L/B/R/F) are shown in different colors and symbols. (f) The four quarters and an inner region (I) discussed in this paper; the radius of the dashed circle is the radius of maximum wind.

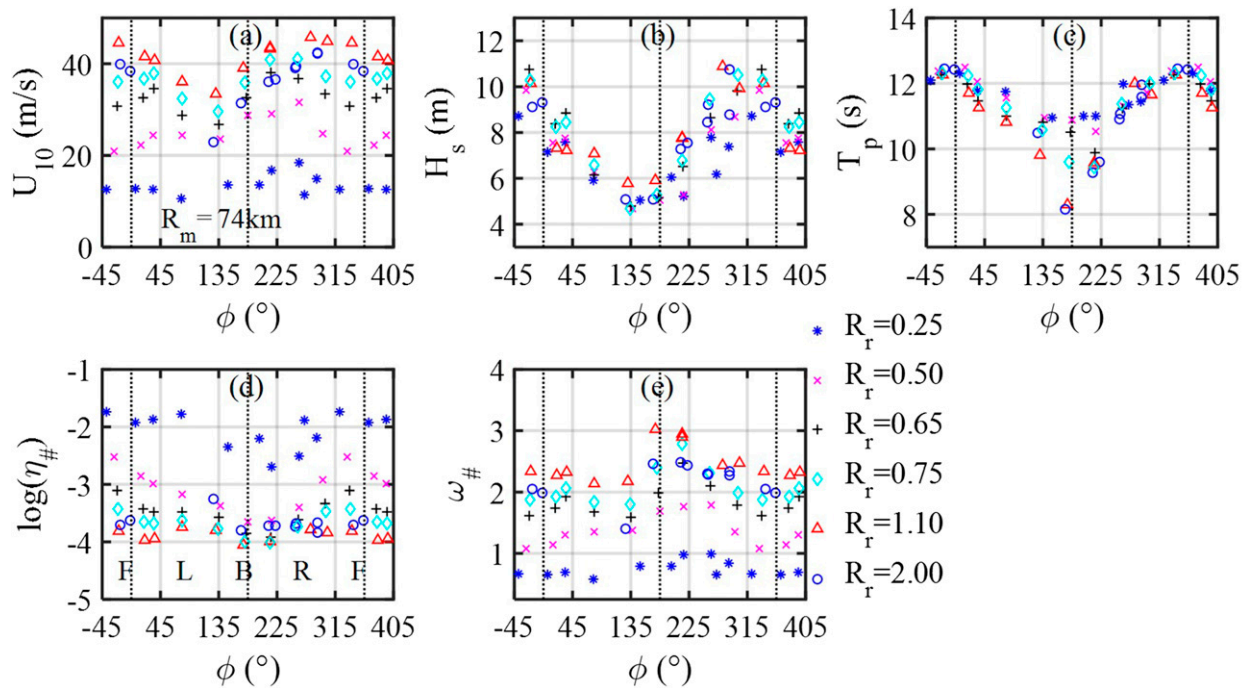


FIG. 3. As in Figs. 1a–e, but plotted with respect to the azimuth angle with respect to the hurricane heading at several radial distances from the hurricane center.

a result of the negative power similarity relationship connecting the two parameters; the subject of similarity is discussed next.

b. Fetch-limited growth functions

The fetch-limited wave growth functions are among the most versatile and robust wind-wave similarity relations. Although theoretical analyses generally assume steady-state and homogeneous wind forcing (e.g., Sverdrup and Munk 1947; Hasselmann et al. 1973; Young and van Vledder 1993; Komen et al. 1994; Young 1999; Janssen 2004; Zakharov 2005; Badulin et al. 2005, 2007; Gagnaire-Renou et al. 2011; Zakharov et al. 2015), the applicability of the established wave growth functions are found to encompass a much wider range of conditions, including rapidly accelerating and decelerating wind fields such as mountain gap winds (e.g., García-Nava et al. 2009; Romero and Melville 2010; Ocampo-Torres et al. 2011; Hwang et al. 2011b) and violent forcing of evolving hurricanes (e.g., Young 1988, 1998, 2003, 2006; Young and Vinoth 2013; Hwang 2016). The range of applicable wavelengths in field observations is also quite broad, extending from the commonly encountered deca- and hectometer scales in the references listed above to meter scale and shorter. For example, the wavelengths produced by $\sim 8.5 \text{ m s}^{-1}$ wind in a sheltered bay during the first 2 h are between 2 and 8 m (Hwang and Wang 2004). Also, Sletten and Hwang (2011) apply the fetch-limited growth functions to the development of decimeter-scale waves generated by a mild breeze ($\sim 3.5 \text{ m s}^{-1}$) to explain the observed difference of approximately 80 to 170 m in the shoreline detection by L- and P-band airborne synthetic aperture radar imagery (Kim et al. 2007); the Bragg resonance wavelengths are 0.19 and 0.55 m, respectively.

The analysis of Hwang (2016) confirms that the waves inside hurricanes (except near the eye region) are in a relatively young stage, and the wave growth can be described by the same functions developed with the steady wind forcing database (e.g., Hwang and Wang 2004; Hwang 2006):

$$\begin{aligned}\eta_{\#} &= 6.19 \times 10^{-7} x_{\#}^{0.81}, & \omega_{\#} &= 11.86 x_{\#}^{-0.24}, \\ \eta_{\#} &= 2.94 \times 10^{-3} \omega_{\#}^{-3.42}.\end{aligned}\quad (1)$$

Figure 4 shows the wind-wave similarity relation $\eta_{\#}(\omega_{\#})$ for several different types of wind forcing conditions, including a dataset combining several field experiments with quasi-steady winds and near neutral stability conditions [Burling 1959; Hasselmann et al. 1973;

Donelan et al. 1985; Dobson et al. 1989; Babanin and Soloviev 1998 (BHDDDB)] and used as the basis for establishing the fetch-limited growth functions by Hwang and Wang (2004); the accelerating and decelerating mountain gap winds in the experiments of García-Nava et al. (2009) (G09) using a moored buoy station and Romero and Melville (2010) (R10) employing the airborne SRA system; the analysis of the combined data is given by Hwang et al. (2011b); and the full set of Hurricane Bonnie 1998 data sorted into the four quarters referenced to the hurricane heading and discussed in this paper (F/L/B/R).

Using the criterion that $\omega_{\#} \approx 0.8$ ($c_p \approx 1.25 U_{10}$) corresponds to the fully developed wave condition (Pierson and Moskowitz 1964), most of the hurricane data inside $r = 30 \text{ km}$ (marked with an x) cannot be considered as local wind generated. The swell contamination is also observed in Young's (1998, 2006) buoy data; see Fig. 4a in Hwang (2016). In contrast to the SRA data with precise localization, buoy data with $\omega_{\#} \leq 0.8$ are probably measurements far away from the hurricane center. The swell contamination will be further discussed in section 2c.

The solid and dashed reference lines in Fig. 4 are the second- and first-order, power-law fitted curves (labeled H04) based on the analysis of the quasi-steady BHDDDB data (Hwang and Wang 2004). We also plotted the growth curves of Hasselmann et al. (1973) (H73) and Donelan et al. (1985) (D85). These curves were used in Young's (1988, 1998, 2006) discussions of hurricane waves. Minor differences of various proposed growth functions have been discussed in great extent (e.g., Donelan et al. 1985; Kahma and Calkoen 1992, 1994; Young 1999; Hwang and Wang 2004; Hwang 2006; Zakharov et al. 2015; and references therein), and they are not repeated here. It is emphasized that the buoy-recorded hurricane datasets reported by Young (1998, 2006) are in very good agreement with the SRA measurements conducted inside hurricanes; see Fig. 4a in Hwang (2016).

Some systematic deviation from the reference curves is detectable for the data groups in the four quarters of the hurricane. In particular, underdeveloped wave variance appear in the left quarter (blue squares) and parts of the back and front quarters (black circles with $\omega_{\#} < \sim 2$ and magenta triangles with $\omega_{\#}$ around ~ 2 ; both groups are from the flight segments that are the farthest from the hurricane center and highlighted with ovals in Figs. 1d and 1e). Overall, the data scatter of the hurricane waves as a whole is comparable to the non-hurricane waves, and they can be described reasonably well by the curves derived from the quasi-steady BHDDDB dataset.

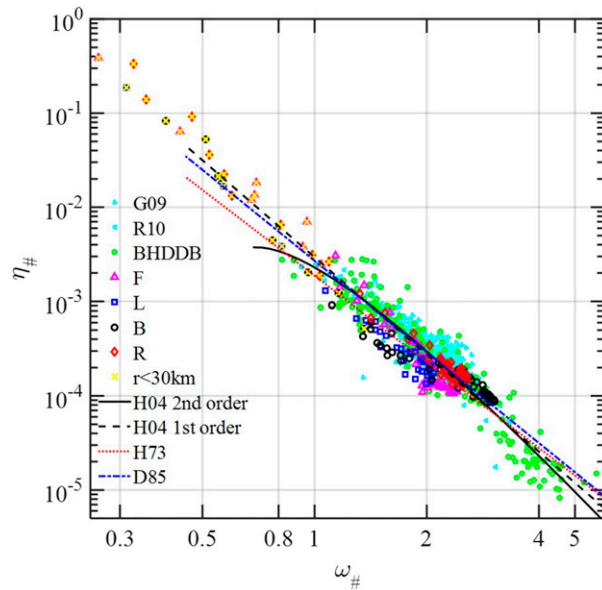


FIG. 4. The wave growth function in terms of $\eta_{\#}(\omega_{\#})$ for the surface waves inside Bonnie 1998. The data are shown with different symbols in four hurricane quarters (L/B/R/F); measurements within the 30-km circle from the hurricane center are marked with an x. On the background with light-colored symbols are the following: BHDDB, data from several field experiments with quasi-steady wind forcing and neutral stability conditions; G09 and R10, rapidly accelerating and decelerating mountain gap winds; and H04, where the solid and dashed lines are the reference curves from second-order and first-order fitting through the BHDDB quasi-steady wind forcing data (Hwang and Wang 2004). For comparison, H73 and D85 are the growth functions of Hasselmann et al. (1973) and Donelan et al. (1985), respectively.

One plausible explanation of the systematic difference observed in the $\eta_{\#}(\omega_{\#})$ relation (Fig. 4) is that the wind generations in different quarters are not on equal footing. With reference to the azimuthal distributions of U_{10} , H_s , and T_p shown in Fig. 3 and focus on the data points at $R_r = 1.1$ (red triangles, radial distance near the local maximum wind speed), the U_{10} ranking for the four quarters is in the order of $R > F > B > L$. For the cyclonic wind forcing, each quarter receives some boost (in the form of preestablished wave field) from the upwind quarter in the order $R \Rightarrow F \Rightarrow L \Rightarrow B \Rightarrow R \dots$. Thus, F is the quarter with the second highest winds and the largest boost from R; L has the lowest winds but good boost from F; and the conditions in both the B and R quarters are much closer to pure local wind generation because of the weaker upstream feeding. The advancing of the hurricane further aids the forward sectors by holding the waves in the generation region longer, whereas in the backward sectors the advancing hurricane decreases the effective wind duration and fetch.

Using the fetch-limited growth functions for the wave variance (or equivalently, significant wave height) and peak wave period, the effective fetch $x_{\eta x}$ and $x_{\omega x}$ can be calculated from the first set of equations in (1) (mks units):

$$\begin{aligned} x_{\eta x} &= 4.24 \times 10^7 U_{10}^{-2.93} H_s^{2.47}, \\ x_{\omega x} &= 2.29 \times 10^4 U_{10}^{-2.22} T_p^{4.22}. \end{aligned} \quad (2)$$

The subscripts ηx and ωx indicate that the associated variables are derived from the functions $\eta_{\#}(x_{\#})$ and $\omega_{\#}(x_{\#})$, respectively. To account for the observed systematic deviation of the hurricane wind waves in different sectors as shown in Fig. 4, the fetches for H_s and T_p are allowed to be different.

The SRA wind-wave triplets provide the necessary measurements on the right-hand side of (2) for investigating the effective fetch inside the hurricane. Figures 5 and 6 show $x_{\eta x}$ and $x_{\omega x}$ calculated along the 10 transects. Making the analogy of a circular race track for the wind blowing inside the hurricane, the effective fetch is expected to increase linearly with the distance from the hurricane center. The computed fetch along each transect (left column of Figs. 5 and 6) is expressed as

$$\begin{aligned} x_{\eta x}(r, \phi) &= a_{\eta x}(\phi)r + A_{\eta x}(\phi), \\ x_{\omega x}(r, \phi) &= a_{\omega x}(\phi)r + A_{\omega x}(\phi). \end{aligned} \quad (3)$$

With kilometers as the unit of r , $x_{\eta x}$, and $x_{\omega x}$ in (3), the azimuthal variations of the slopes ($a_{\eta x}$ and $a_{\omega x}$) and intercepts ($A_{\eta x}$ and $A_{\omega x}$) from least squares fitting are shown in the right columns of Figs. 5 and 6 and as lookup tables (LUTs) in Table 1. The formulas may produce negative fetch in some azimuth angles for small r values, so an additional condition of minimum fetch value is imposed. Several values between 1 and 50 km were tested for the minimum fetch, and they only produced minor differences in the resulting wave computation near the hurricane center, mainly because the number of instances of negative fetches of the preconditioned formulas is small. The results presented below are based on a minimum fetch of 5 km.

Using (3), the effective fetch for any location inside the hurricane can be calculated. Applying to the Bonnie 1998 measurements, the results of the fetch growth of wave variance and wave period are shown in Fig. 7. For comparison, the nonhurricane datasets displayed in Fig. 4 are also plotted in the background. Excluding those data points near the eye region (marked by x and + for $r < 30$ and $30 \leq r < 45$ km, respectively), the

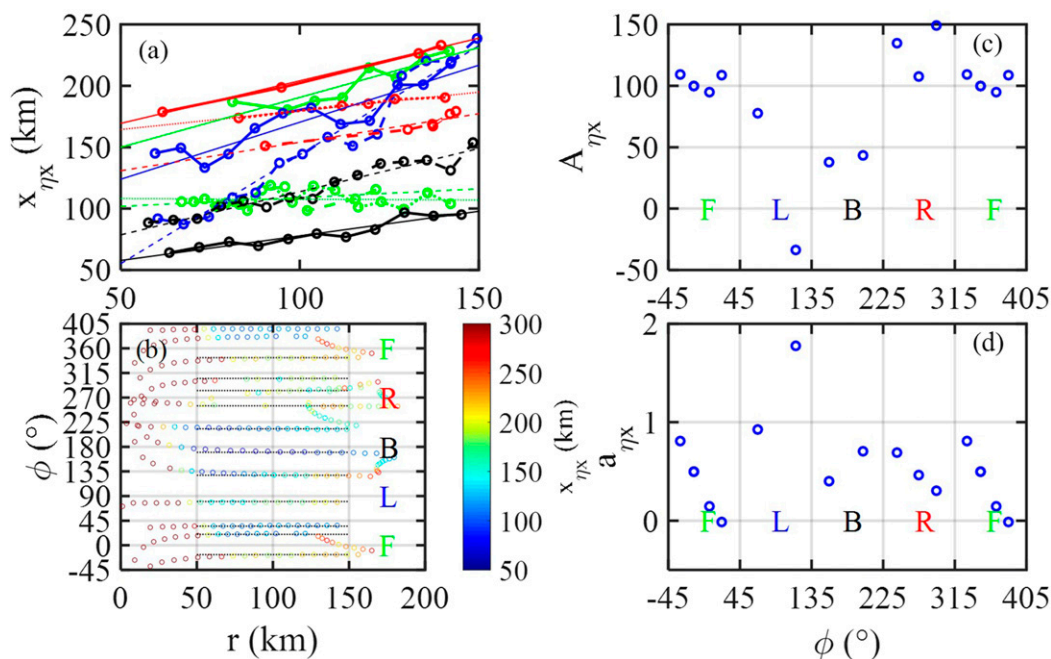


FIG. 5. The effective fetch for significant wave height computed from the wind and wave data along 10 transects: (a) the results are shown as a function of r in four different quarters with different colors (blue/black/red/green for L/B/R/F); (b) the magnitude of the fetch is color coded and plotted as a function of r and ϕ ; and (c) the intercept A and (d) slope a of the fitted linear function relating the fetch and the radial distance.

data scatter of the wind waves inside the hurricane is not worse than those generated in nonhurricane conditions, and the same functions established for steady wind forcing conditions are applicable to the wave growth inside the hurricane.

c. Wind-wave triplets and fetch growth functions

The fetch-limited growth functions can be used to estimate the key wave parameters of significant wave height and dominant wave period, given the knowledge

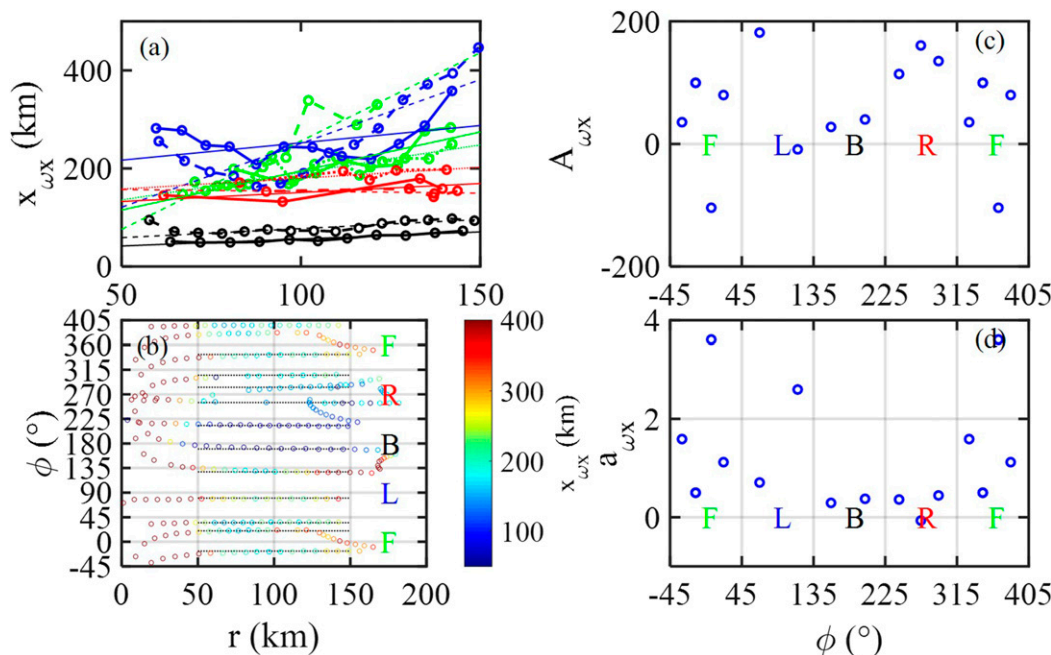


FIG. 6. As in Fig. 5, but for the fetch of spectral peak wave period.

TABLE 1. Lookup tables for the effective fetches $x_{\eta x}$ and $x_{\omega x}$.

ϕ (°)	$A_{\eta x}$ (km)	$a_{\eta x}$	$A_{\omega x}$ (km)	$a_{\omega x}$
-13	100.00	0.50	100.00	0.50
7	94.72	0.14	-104.50	3.60
22	108.79	-0.01	79.43	1.12
67	77.47	0.93	181.65	0.71
115	-33.58	1.78	-9.26	2.60
157	37.75	0.40	27.46	0.29
200	43.45	0.70	40.29	0.37
242	134.73	0.69	114.20	0.37
270	107.65	0.46	160.67	-0.07
292	149.25	0.30	135.62	0.45
330	109.42	0.81	35.62	1.59
347	100.00	0.50	100.00	0.50
367	94.72	0.14	-104.50	3.60

of wind speed and wind fetch as a function of position inside the hurricane (Hwang 2016):

$$H_{sw} = 8.10 \times 10^{-4} U_{10}^{1.19} x_{\eta x}^{0.405},$$

$$T_{pw} = 9.28 \times 10^{-2} U_{10}^{0.526} x_{\omega x}^{0.237}. \quad (4)$$

The subscript w is appended to the wave variables in (4) to emphasize that the wind-sea portion is obtained with the fetch-limited wave growth functions. The computed H_{sw} and T_{pw} are compared to the SRA in situ measurements of H_s and T_p in Fig. 8, showing the ratios $R_{HU} = H_{sw}(U_{10}, x_{\eta x})/H_s(\text{SRA})$ and $R_{TU} = T_{pw}(U_{10}, x_{\omega x})/T_p(\text{SRA})$ plotted as functions of r on the left column and as functions of ϕ on the right column. Excluding the region close to the hurricane center, the ratios generally stay within 1.00 ± 0.10 , indicating wind-sea dominance in most of the hurricane coverage area.

During the period of data acquisition, the radius of maximum wind speed r_m is about 74 km, as documented in Table 1 of Moon et al. (2003). The result shown in the left column of Fig. 8 indicates that local wind waves dominate from outward of slightly less than r_m and to at least $2.5r_m$ distance from the hurricane center (the maximum range of the SRA data). There are some exceptions: in the outer region of the front quarter for the wave height (the green triangles near $r = 120$ to 160 km in Fig. 8a; corresponding to the data points in the upper ovals in Figs. 1d and 1e) and the outer region of the back quarter for the wave period (the black circles near $r = 165$ to 180 km in Fig. 8b; corresponding to the data points in the lower ovals in Figs. 1d and 1e). Inside the circle of maximum wind speed, $r < r_m = 74$ km, local wind waves remain dominant to about 50 km; farther inward, the swell contribution increases steadily, particularly in the front quarter for wave height (Fig. 8a) and left quarter for wave period (Fig. 8b).

Excluding the region close to the hurricane center, the ratios generally stay within 1.00 ± 0.10 . Specifically, for $r > 75$ km, the average and standard deviation of R_{HU} and R_{TU} are 1.00 ± 0.089 and 0.99 ± 0.069 . The corresponding statistics of SRA-measured H_s and T_p are 7.77 ± 1.85 m and 10.86 ± 1.27 s; the fetch-law-computed H_{sw} and T_{pw} are 7.73 ± 1.77 m and 10.77 ± 1.33 s.

Alternatively, using the fetch-limited growth functions, the wind speed can be obtained from H_s or T_p accompanied with the fetch input (Hwang 2016):

$$U_{10} = 397.46 H_s^{0.841} x_{\eta x}^{-0.341},$$

$$U_{10} = 91.49 T_p^{1.900} x_{\omega x}^{-0.450}. \quad (5)$$

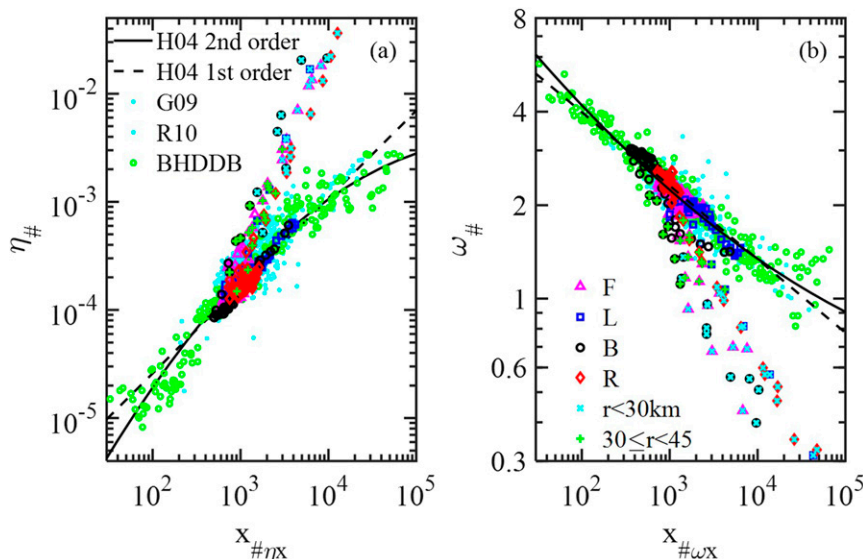


FIG. 7. As in Fig. 4, but in terms of the fetch-limited growth functions of (a) $\eta_{\#}(x_{\#})$ and (b) $\omega_{\#}(x_{\#})$.

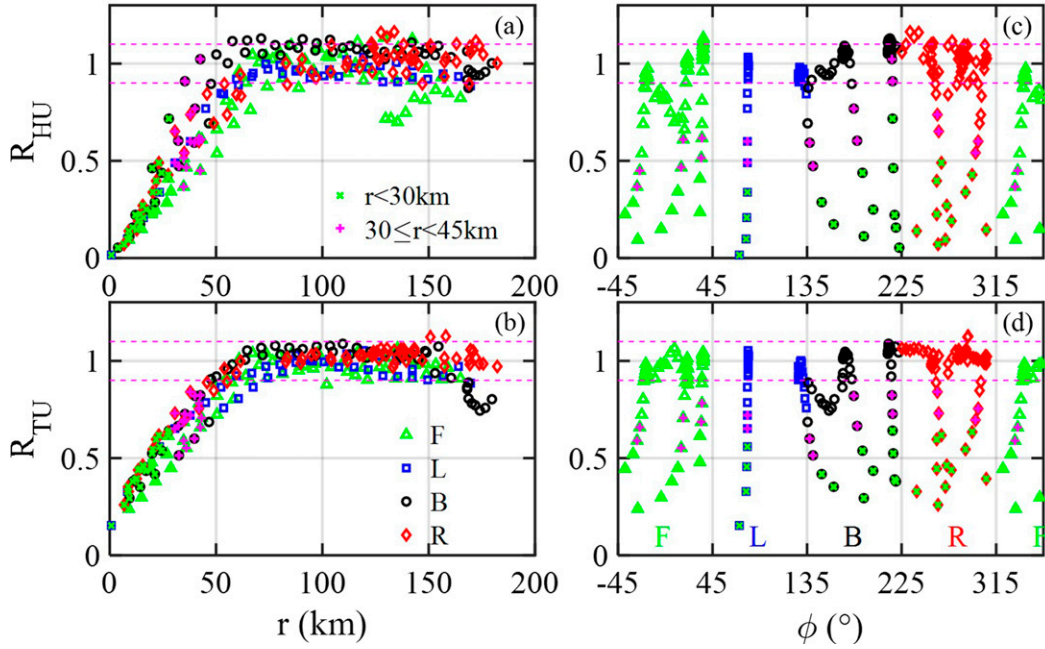


FIG. 8. (top) The ratio between the H_{sw} computed with U_{10} and the $\eta_{\#}(x_{\#})$ growth function and the SRA-measured H_s , plotted against (a) r and (b) ϕ . (bottom) As in the (top), but for T_{pw} computed with U_{10} and the $\omega_{\#}(x_{\#})$ growth function, plotted against (c) r and (d) ϕ .

Figure 9 shows the ratios $R_{UH} = U_{10}(H_s, x_{\eta_{\#}})/U_{10}(\text{HRD})$ and $R_{UT} = U_{10}(T_p, x_{\omega_{\#}})/U_{10}(\text{HRD})$. In the same format of Fig. 8, the results are plotted as functions of r on the left column and as functions of ϕ on the right column.

Similar to the results of R_{HU} and R_{TU} , the ratios R_{UH} and R_{UT} deviate from unity inward of $r < 50$ km due to the mixed sea condition. For $r > 75$ km, it is wind-sea dominance; the average and standard deviation of R_{UH}

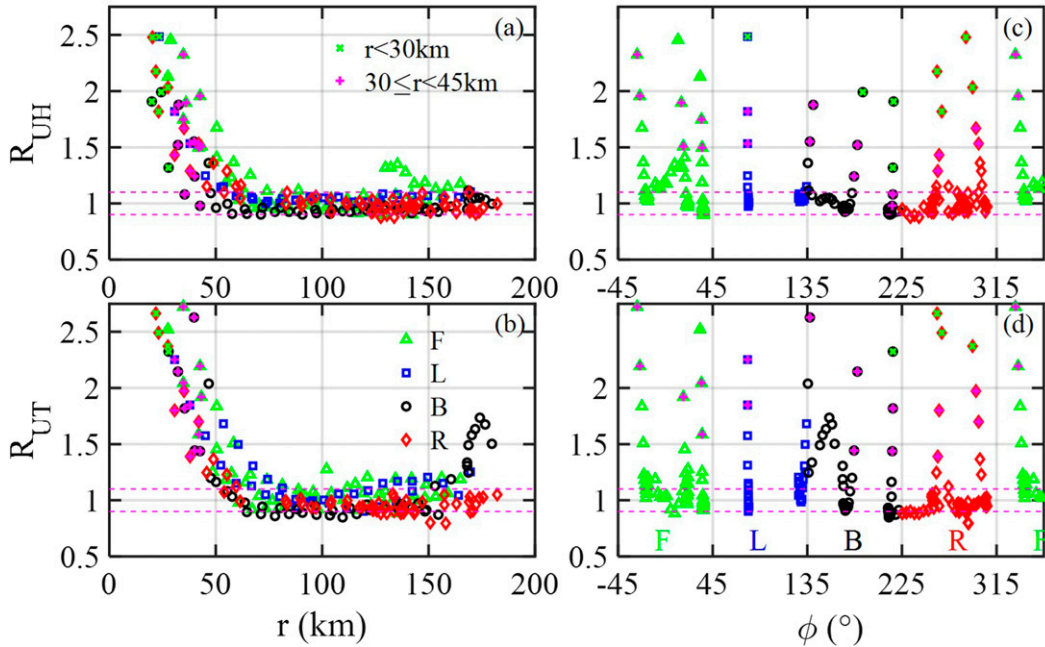


FIG. 9. As in Fig. 8, but for comparison of the reference HRD U_{10} with the U_{10} retrieved from H_s and T_p combined with fetch by using the wave growth functions.

and R_{UT} are 1.00 ± 0.083 and 1.03 ± 0.16 . The corresponding statistics of HRD U_{10} versus H_s - and T_p -derived U_{10} are 37.38 ± 6.15 versus 37.46 ± 6.72 and $37.70 \pm 6.15 \text{ ms}^{-1}$. As noticed before (Hwang 2016), the wind speed inversion using T_p is not as good as the result using H_s . This is probably caused by the relatively coarse wavenumber resolution of the SRA measurement; that is, the wavenumber resolution of the SRA wave spectra is limited by the narrow swath ($\sim 1200 \text{ m}$).

3. Air-sea exchange

a. Asymmetric distribution

From the energy balance equation, the total (frequency integrated) rate of wind energy input through the surface wave motion is expressed as a combination of the wind-wave triplets (Hwang and Sletten 2008):

$$E_t = \alpha_E \rho_a U_{10}^3; \quad \alpha_E = 0.20 \omega_{\#}^{3.3} \eta_{\#}. \quad (6)$$

A similar expression can be derived for the momentum exchange (see the appendix):

$$M_t = \alpha_M \rho_a U_{10}^2; \quad \alpha_M = 0.40 \omega_{\#}^{4.3} \eta_{\#}. \quad (7)$$

Using the procedure described in section 2c, the necessary wave information can be calculated from the hurricane wind field, which is the data most likely available among the three wind-wave parameters (U_{10} , H_s , and T_p). Here, we present the results of a case study. Figure 10a shows the HRD wind field at 1830 UTC 24 August 1998, which is the closest time to the SRA measurements (2030 UTC 24 August to 0144 UTC 25 August) with the gridded data available at the archive site. The maximum, 1-min, sustained surface wind speed is about 44 ms^{-1} (category 2) at 95 km northeast (NE) of center.

Using the effective fetch equations in (3) and fetch-limited wave growth functions in (4), the computed H_{sw} , T_{pw} , $\eta_{\#}$, and $\omega_{\#}$ are illustrated in Figs. 10b–e. The azimuthal and radial variations of the wind-wave triplets and the corresponding dimensionless $\eta_{\#}$ and $\omega_{\#}$ show rather complex patterns. In general terms, the wave height is higher on the right-hand side, the wave period is longer in the front quarter, the young seas (high $\omega_{\#}$) are in the rear quarter, and the older seas (low $\omega_{\#}$) occupy the left half plane.

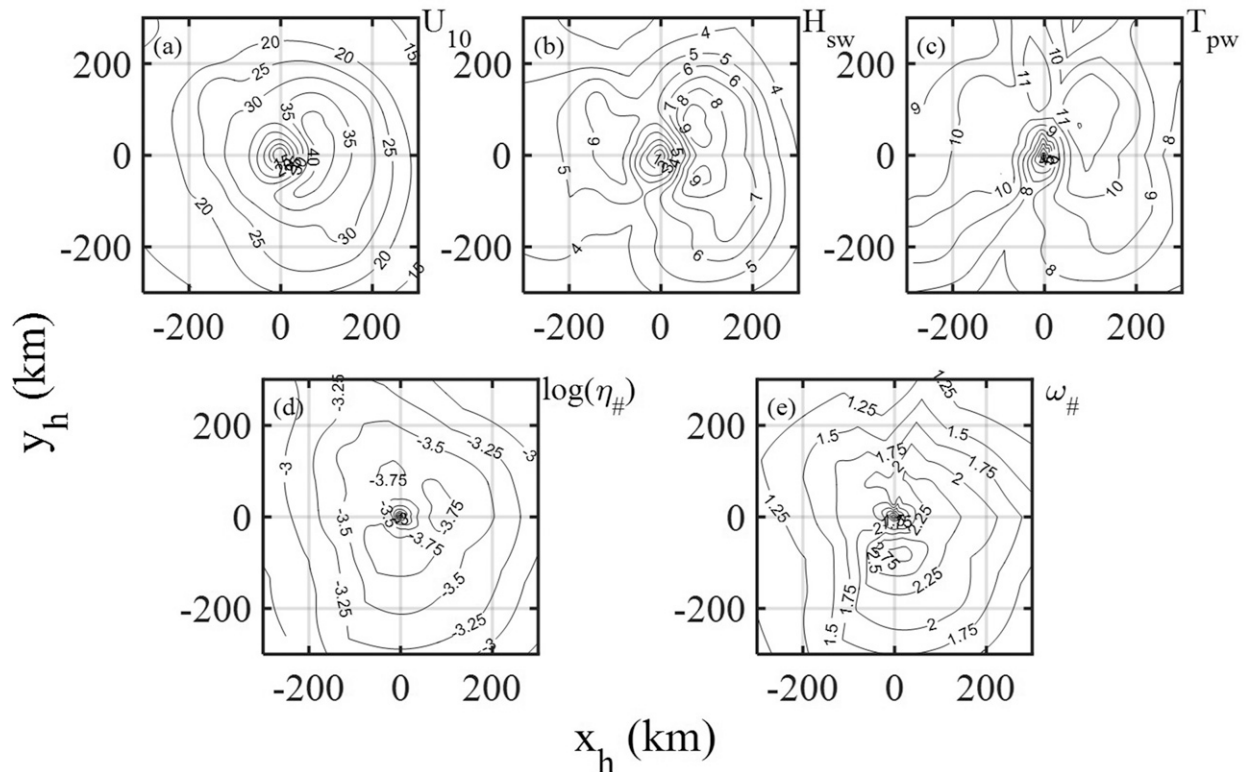


FIG. 10. An example illustrating the application of the wind-wave growth functions to derive wave properties from the hurricane wind field: (a) the input HRD U_{10} field for Hurricane Bonnie at 1830 UTC 24 Aug 1998, the output includes wave fields of (b) H_{sw} and (c) T_{pw} , and the dimensionless wind-wave parameters (d) $\eta_{\#}$ and (e) $\omega_{\#}$.

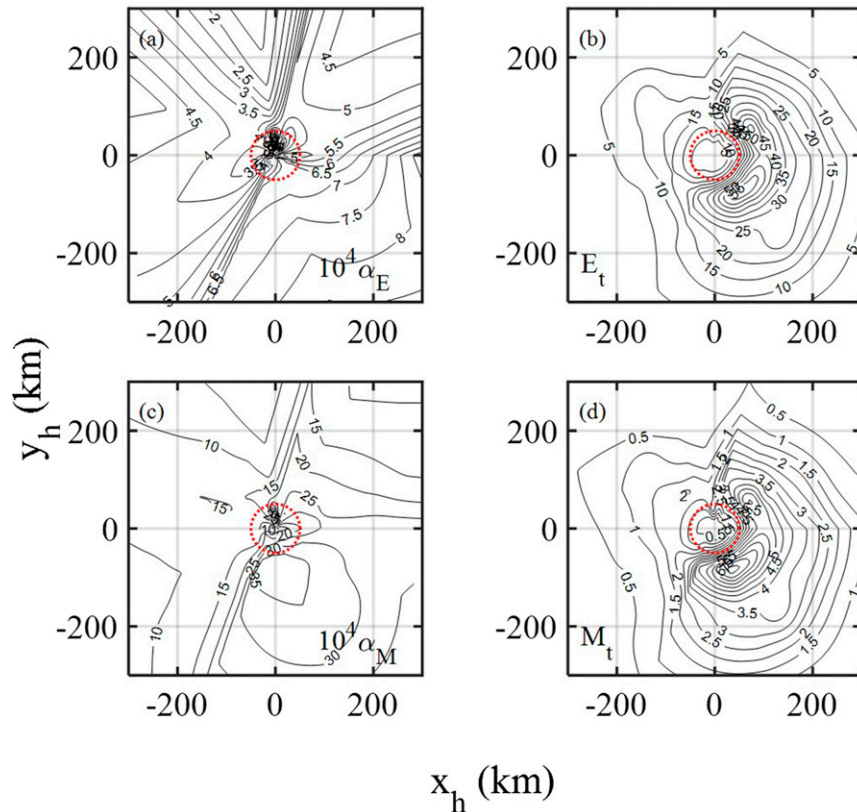


FIG. 11. The computed energy and momentum exchange properties inside a hurricane: (a) α_E , (b) E_t , (c) α_M , and (d) M_t . The radius of the dotted circle is 50 km.

Figure 11 shows the energy and momentum exchange computations. The exchange coefficients α_E and α_M are given in the left column, and the exchange rates E_t and M_t are in the right column. The most intensive air–sea interaction in terms of the exchange coefficients is taking place in the back quarter and the right rear segment of the hurricane, spanning over the azimuth angles approximately between 150° and 270° (Figs. 11a, 11c). The exchange rates are weighted by the wind speed, cubic for energy and quadratic for momentum; the E_t and M_t spatial patterns show two islands at the right-front and right-back of the hurricane at the radial distance near the wind speed maximum (Figs. 11b, 11d).

Integrated over the circle of 250-km radius (at which distance, the U_{10} is still well above 15 m s^{-1} ; Fig. 10a) and denoting A as the integration area, the $E_t A$ and $M_t A$ are 3.33 TW and 0.44 TN, of which 2.44 TW and 0.31 TN are on the right half, and 0.89 TW and 0.12 TN are on the left half. If the line along 150° and 330° is used to separate the two half planes, the right- and left-half exchanges are 2.46 TW and 0.33 TN and 0.87 TW and 0.11 TN, respectively. On average, the total exchanges on the right-hand side are about 3 times those on the left-hand side.

As discussed earlier regarding Fig. 8, H_s and T_p obtained from the fetch growth functions are the wind-sea components, and for $r < \sim 50 \text{ km}$, they are significantly different from the SRA measurements as a result of swell contamination. We emphasize that computations of (6) and (7) use the wind-sea components of H_s and T_p . It may not be feasible to separate wind sea and swell from the measured wave spectrum, which may be overwhelmed by swell. Therefore, the computation of energy and momentum exchanges near the eye region is less reliable using in situ observation of H_s and T_p . A red, dotted circle with $r = 50 \text{ km}$ is added in each panel of Fig. 11. On the other hand, for the 250-km radius of hurricane coverage, the 50-km circle represents 4% of the coverage area. With relatively low wind speeds, the area contributes only slightly to the overall energy and momentum exchanges. For the present case (computed with the wind-sea components, in principle), $E_t A$ and $M_t A$ integrated over the 50-km circle around the eye are 49.7 GW and 8.71 GN (or 1.49% and 1.98%) of the total over the 250-km circle.

The wave modification on the azimuthal and radial distributions of the momentum and energy exchanges is quite significant. For example, if the air–sea exchanges are

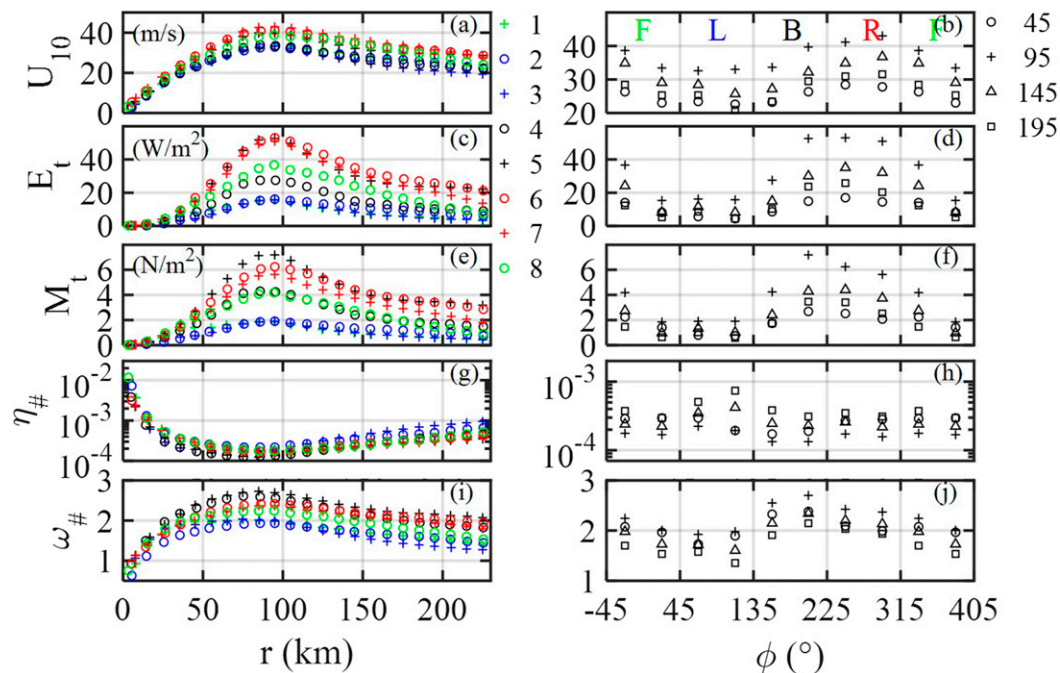


FIG. 12. (left) Radial and (right) azimuthal variations of (a),(b) U_{10} , (c),(d) E_t , (e),(f) M_t , (g),(h) $\eta_{\#}$, and (i),(j) $\omega_{\#}$ inside a hurricane; all parameters are averaged over 45° azimuth slices. The number in the legend for the left column is in the sequence of the 45° slice referenced to the hurricane heading, increasing CCW; the numbers in the legend for the right column are the radial distance in km from the hurricane center.

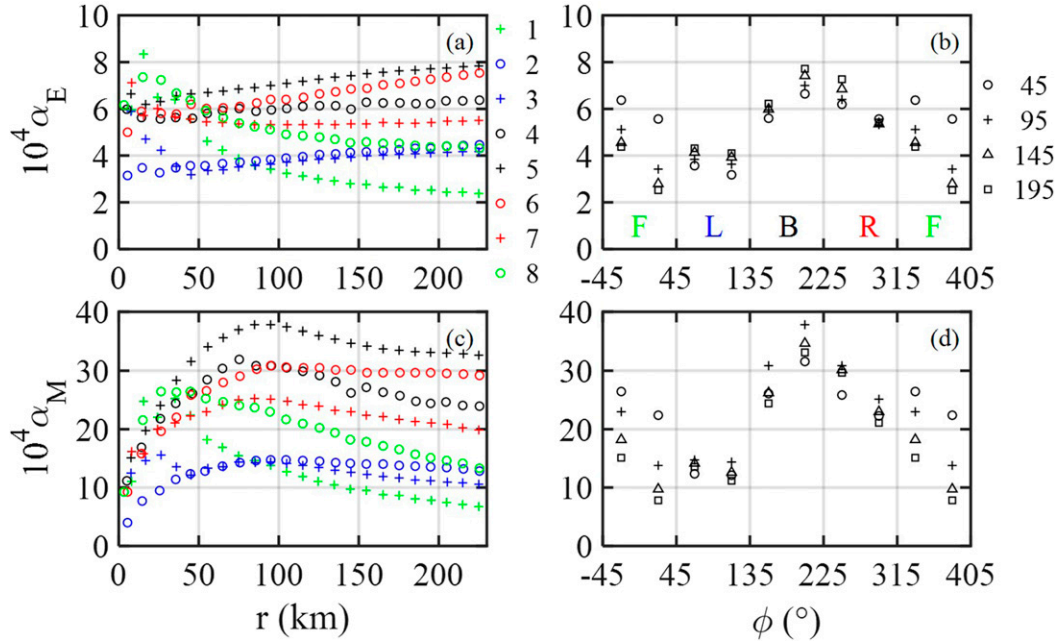
evaluated with the wind speed alone without considering the wave properties, the total ($\rho_a \langle \alpha_E \rangle U_{10}^3 A$, $\rho_a C_{10} U_{10}^2 A$) integrated over the 250-km circle are 2.84 TW and 0.44 TN, of which 1.87 TW and 0.26 TN are on the right half plane and 0.97 TW and 0.17 TN are on the left half plane; the right to left ratios are about 2:1 to 3:2 from wind speed consideration alone, instead of 3:1 when the wave properties are accounted for in the exchange computation. In the above computation using U_{10} alone, the drag coefficient C_{10} is calculated by (8), which is discussed in the next subsection, and the representative energy exchange coefficient is given as $\langle \alpha_E \rangle = 4.7 \times 10^{-4}$ (Hwang and Sletten 2008; Hwang 2009).

Dividing the circular area into eight 45° pie slices, the left column of Fig. 12 shows the smoothed view of the complex radial variations of U_{10} , E_t , M_t , $\eta_{\#}$, and $\omega_{\#}$. Slices 1, 2, 3, and 4 are on the left-hand side of the hurricane starting from front to back referenced to the hurricane heading; slices 5, 6, 7, and 8 are on the right-hand side from back to front. The right column shows the azimuthal distribution at four radial distances: 45, 95, 145, and 195 km. The locations of maximum wind speed in the eight pie slices remain at a similar radial distance from the hurricane center (about 90 to 95 km). The azimuthal location of the maximum wind speed is near $\phi = 290^\circ$, whereas the maxima of energy and momentum exchanges are close to about $\phi = 225^\circ$

(Figs. 12b, 12d, 12f). This phase shift reflects the strong impact on the E_t and M_t values by the wave factors expressed as dimensionless frequency and dimensionless variance [(5) and (6)]. In other words, the azimuthal phase shift between the distributions of U_{10} , E_t , and M_t reflects the radial and azimuthal variations of the exchange coefficients α_E and α_M , as illustrated in Fig. 13 in the same format of Fig. 12, showing the dependence on the radial distance in the left column and the dependence on the azimuth angle in the right column. The peaks are at about $\phi = 200^\circ$ for α_E and α_M (Figs. 13b, d), whereas the peak of U_{10} is at about 290° (Fig. 12b). Similar to the discussion of Fig. 11, the computations of energy and momentum exchanges near the eye region ($r < \sim 50$ km) are less reliable because of the mixed sea condition, although the present computation is done with the wind-sea components in principle.

b. Momentum exchange and wind stress

The momentum exchange coefficient α_M can be compared to the surface drag coefficient (see the appendix). There are many papers devoted to the study of the drag coefficient. Figure 14 shows several field datasets with emphasis on high wind conditions. The solid line is the fitted curve using the open-ocean data marked “FPJ” (Felizardo and Melville 1995; Powell

FIG. 13. As in Fig. 12, but for (a),(b) α_E and (c),(d) α_M .

et al. 2003; Jarosz et al. 2007) as discussed in Hwang (2011) and Hwang et al. (2013):

$$C_{10} = 10^{-5}(-0.16U_{10}^2 + 9.67U_{10} + 80.58). \quad (8)$$

Additional drag coefficient data collected inside hurricanes (Powell 2006; Holthuijsen et al. 2012) are added (labeled P06 and H12, respectively) in the figure. The P06 data are sorted into two groups inside

and outside the 30-km circle from the hurricane center. The drag coefficients for the inside group are considerably lower than those of the outside group. The H12 data include the average of a large number (1452) of wind profile analyses as well as subgroups sorted into left, right, and rear (back) sectors with respect to the hurricane heading. These drag coefficient data under hurricane conditions demonstrate the large variability but with the general trend consistent with (8).

We processed the α_M result given in Fig. 11d to show the overall average and the mean values in the left, back, and right sectors in a similar fashion of H12 results (Holthuijsen et al. 2012). Given the large scatter of the experimental data, the computed momentum exchange coefficient based on the fetch-limited wave growth functions seems to show significant agreement with the field observations of the drag coefficient inside hurricanes. Additional discussion between the momentum exchange coefficient and the drag coefficient is given in the appendix.

4. Summary

The robust wind-wave growth functions established with ideal fetch-limited and quasi-steady wind forcing conditions are also applicable to wind-generated waves under considerably more varying conditions, including hurricanes (Young 1988, 1998, 2003, 2006; Young and Vinoth 2013; Hwang 2016) and rapidly accelerating and

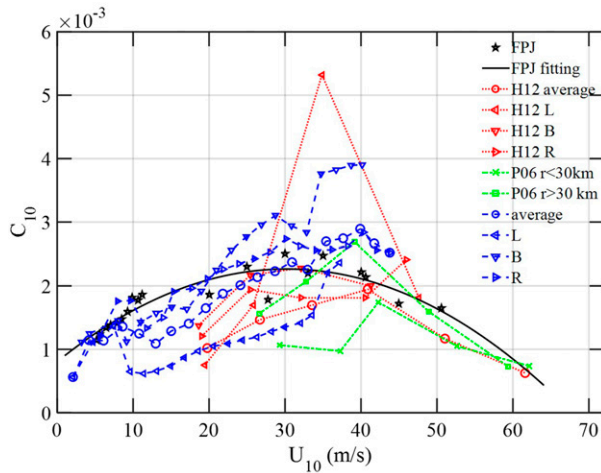


FIG. 14. Comparison of the momentum exchange coefficient α_M (blue symbols) with field observations of drag coefficient C_{10} emphasizing data collected in hurricane conditions (black, red, and green symbols).

decelerating wind fields such as those encountered in mountain gap winds (García-Nava et al. 2009; Romero and Melville 2010; Ocampo-Torres et al. 2011; Hwang et al. 2011b). The robust similarity functions scale with local wind and wave properties (U_{10} , H_s , and T_p) for both steady and unsteady or homogeneous and inhomogeneous wind forcing conditions and may suggest that local balance (temporally and spatially) plays a dominant role in the air–sea energy and momentum exchanges.

With the deployment of SRA in hurricane hunter missions, the detailed 2D wavenumber spectra have advanced significantly our understanding of the wave conditions inside hurricanes. In a recent paper (Hwang 2016), the fetch- and duration-limited nature of wave development inside hurricanes was investigated with 60 wave spectra collected during Bonnie 1998 (Wright et al. 2001) and 12 wave spectra collected during Ivan 2004 (Black et al. 2007). These measurements provide sufficient information for sorting the wave development into three azimuthal sectors.

The full suite of the SRA measurements during the particular Bonnie 1998 mission contains 233 wave spectra along 10 transects radiating from the hurricane center. The full dataset offers the opportunity to examine the complex azimuthal and radial variation of the wind-generated waves inside the hurricane with considerably better resolution. Lookup tables (Table 1) are produced for the location-dependent effective fetches of significant wave height and spectral peak wave period [(3)]. Using the fetch model, the wind-wave triplets U_{10} , H_s , and T_p can be calculated with the fetch-limited growth functions, knowing only one of the three variables [(4) and (5)]. The results show the dominance of the wind-sea condition in the broad region of the hurricane interior; for the case studied in this paper, it is approximately from 50 km outward to the maximum distance available in the SRA data (about 180 km from the hurricane center). The fetch-limited growth functions yield good results, generating the full suite of the wind-wave triplets given only one of the three variables (Figs. 8, 9).

The frequency-integrated air–sea energy and momentum exchange through the wave action can be estimated with the parameterization functions [(6) and (7)]. The results show significant azimuthal and radial variations (Figs. 11–13). For the case studied here, the air–sea energy and momentum exchanges in the right half plane of the hurricane is about 3 times stronger than those in the left half plane. The degree of asymmetry is considerably stronger than the momentum and energy exchange estimation using the wind speed parameter alone. The momentum exchange coefficient

α_M computed with the wind-sea growth functions can be considered the drag coefficient expressed as C_{10} or $C_{\lambda/2}$; the latter expression generally yields less data scatter (Figs. 14, A1).

In summary, making use of the robust, fetch-limited nature of surface waves generated by the hurricane winds, the azimuthal and radial variations of the wind and wave properties and the associated parameters, such as E_t and M_t in the interior of the hurricane coverage area, can be studied in great detail; the necessary input for the computation can be as few as only one of the three wind-wave triplets (U_{10} , H_s , and T_p) coupled with the fetch or duration model.

Acknowledgments. This work is sponsored by the Office of Naval Research (PH: Doc. N0001416WX00044). We are grateful for the service of HRD wind archive maintained in the HWind legacy data site (http://www.hwind.co/legacy_data/). Datasets used in this analysis are given in the cited references. The processing codes and data segments can also be obtained by contacting the corresponding author.

APPENDIX

Parameterization of Air–Sea Energy and Momentum Fluxes

Hwang and Sletten (2008) present a parameterization equation of the air–sea energy exchange rate through the wave motion E_t , which is computed by

$$E_t = \frac{dE}{dt} = \int_0^\infty \rho_w g Q_{in} d\omega, \quad (A1)$$

where ρ_w is the density of water, and Q_{in} is the wind input source function in the wave energy balance equation. The source function is generally written as

$$Q_{in} = \gamma_{in} s \omega \chi(\omega), \quad (A2)$$

where γ_{in} is the nondimensional wind input coefficient, $s = \rho_a/\rho_w$ is the ratio of air and water densities, and $\chi(\omega)$ is the wave spectral density. Carrying out the integration over frequency and denoting the resulting quantity with angular brackets, (A1) becomes

$$E_t = \rho_w g s \langle \gamma_{in} \rangle \omega_p S = s \langle \gamma_{in} \rangle \omega_p E, \quad (A3)$$

where S is the wave variance, which relates to the wave energy by $E = \rho_w g S$.

In the dimensionless form scaled by wind speed, (A3) becomes

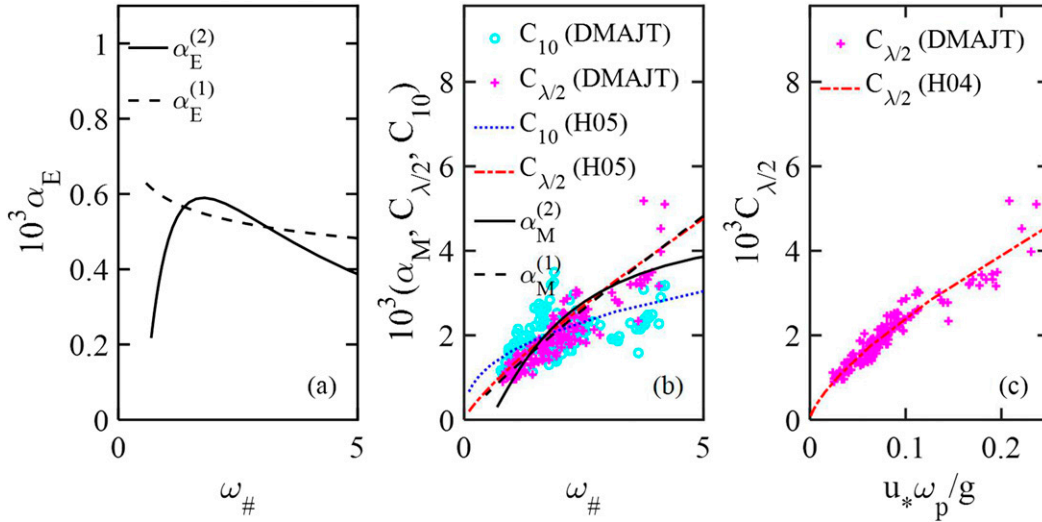


FIG. A1. (a) α_E and (b) α_M dependence on $\omega_{\#}$ computed with the first- and second-order, fitted, wind-wave growth functions. In (b), the ocean surface drag coefficient (given as C_{10} and $C_{\lambda/2}$) measured under wind-sea dominant conditions are superimposed; the similarity relation of the drag coefficient is best represented as (c) $C_{\lambda/2}(u_* \omega_p / g)$; see text for more detail.

$$E_t / (\rho_a U_{10}^3) = \langle \gamma_{in} \rangle \omega_{\#} \eta_{\#}. \quad (\text{A4})$$

Making computations using several published formulas of γ_{in} and assuming power function for the elevation spectrum with the spectral slope between -4 and -5 , the ensemble average produces

$$\langle \gamma_{in} \rangle = 0.20 \omega_{\#}^{2.3}. \quad (\text{A5})$$

The frequency-integrated energy input from wind to the wave field is therefore

$$\begin{aligned} E_t &= 0.20 \omega_{\#}^{3.3} \eta_{\#} \rho_a U_{10}^3 = \alpha_E \rho_a U_{10}^3; \\ \alpha_E &= 0.20 \omega_{\#}^{3.3} \eta_{\#}. \end{aligned} \quad (\text{A6})$$

Because the energy for wave growth represents a small portion—less than about 10%, wave age dependent (see Fig. 2 of Hwang and Sletten 2008)—the frequency-integrated energy input is balanced predominantly by the energy dissipation (Phillips 1985), which is contributed mainly by wave breaking; (A6) is a good approximation for the breaking energy dissipation rate of a wave field.

The wave momentum M and wave energy E are closely associated, for a sinusoidal motion with phase speed c , $E = Mc$, or in spectrum form $\chi_E(\omega) = \chi_M(\omega)c(\omega)$, where subscripts E and M represent energy and momentum, respectively (e.g., Dean and Dalrymple 1991). The momentum spectrum can be obtained from the wave elevation spectrum by $\chi_M(\omega) = \chi_E(\omega)\omega g^{-1}$, where deep-water dispersion relation is used ($c = g\omega^{-1}$). We can go through the same procedure above for E_t to produce an equivalent M_t parameterization function. The following

describes an alternative approach to find the ratio $R_{ME} = M_t/E_t$ and to make use of the existing E_t parameterization for quantifying M_t .

Using a popular and simple wind input growth rate formula (Plant 1982; Phillips 1985)

$$\beta = \gamma_{in} s \omega = X_1 \omega (u_*/c)^2, \quad (\text{A7})$$

where X_1 has a numerical value close to 0.04, we can write M_t and E_t as follows:

$$E_t = \int_0^\infty \rho_w g X_1 u_*^2 (\omega^2/g^2) \chi(\omega) d\omega, \quad \text{and} \quad (\text{A8})$$

$$M_t = \int_0^\infty \rho_w g X_1 u_*^2 (\omega^3/g^3) \chi(\omega) d\omega. \quad (\text{A9})$$

Because the dominant contribution of the two integrations comes from the high-frequency portion of the wave spectrum, we evaluate R_{ME} with integration from ω_p to $N\omega_p$, where N is a large number. Expressing the high-frequency portion of the spectrum as a power function, $\chi(\omega) \sim \omega^a$, with a between -4 and -5 ; for $a = -4$, the ratio is

$$R_{ME} = (\omega_p/g) \ln N. \quad (\text{A10})$$

The value of N is suggested to be between 5 and 10 by Hwang and Sletten (2008), which gives $\ln 5 = 1.6$ and $\ln 10 = 2.3$.

For $a \neq -4$, integrating from ω_p to ∞ yields

$$R_{ME} = (\omega_p/g) \frac{a+3}{a+4}. \quad (\text{A11})$$

For $a = -5$, $(a+3)(a+4)^{-1} = 2$. Using the value $R_{ME} \approx 2\omega_p g^{-1}$, the parameterization of the rate of momentum exchange thus becomes

$$M_t = 2(\omega_p/g)E_t, \quad (\text{A12})$$

which can be written as

$$M_t = \alpha_M \rho_a U_{10}^2; \quad \alpha_M = 0.40\omega_{\#}^{4.3}\eta_{\#}. \quad (\text{A13})$$

Figure A1 plots $\alpha_E(\omega_{\#})$ and $\alpha_M(\omega_{\#})$ using both first- and second-order fitted growth functions. Because $\eta_{\#} = 2.94 \times 10^{-3}\omega_{\#}^{-3.42}$ [(1)] to the first order, α_E is almost constant ($\alpha_E = 5.88 \times 10^{-4}\omega_{\#}^{-0.12}$) and α_M varies with $\omega_{\#}$ almost linearly ($\alpha_M = 1.18 \times 10^{-3}\omega_{\#}^{0.88}$).

The momentum exchange coefficient α_M is closely related to the ocean surface drag coefficient. Superimposed on Fig. A1b are the drag coefficient data from five field experiments conducted under wind-sea dominant conditions; together they cover a wide range of the dimensionless wave age. These measurements are labeled DMAJT for Donelan (1979), Merzi and Graf (1985), Anttil and Donelan (1996), Janssen (1997), and Terray et al. (1996).

Hwang (2004) shows that for wind sea the similarity relation of the ocean surface drag coefficient exists in the form $C_{\lambda/2}(u_*\omega_p/g)$: $C_{\lambda/2} = 1.22 \times 10^{-2}(u_*\omega_p/g)^{0.704}$ (Fig. A1c), where $C_{\lambda/2}$ is the drag coefficient referenced to the wind speed at the elevation one-half of the peak wavelength, and u_* is the wind friction velocity.

The data scatter increases when the drag coefficient is given as $C_{\lambda/2}(\omega_{\#}) = C_{\lambda/2}(U_{10}\omega_p/g)$; the correlation deteriorates further when given as $C_{10}(\omega_{\#}) = C_{10}(U_{10}\omega_p/g)$ (Fig. A1b). The least squares fitted curves through the data are $C_{\lambda/2} = 1.289 \times 10^{-3}\omega_{\#}^{0.815}$ and $C_{10} = 1.632 \times 10^{-3}\omega_{\#}^{0.391}$ (Hwang 2005a). Interestingly, the fitted curve of $C_{\lambda/2}(\omega_{\#})$ (red dotted-dashed line) is almost identical to the momentum exchange coefficient computed with the first-order fitted wave growth function $\alpha_M^{(1)}(\omega_{\#})$ (black dashed line).

More extensive discussions on the dimensionally consistent and inconsistent expressions of the ocean surface drag coefficient for both the wind sea and mixed sea are given in Hwang (2005a, b), Hwang et al. (2011a), and many additional references cited in those studies.

REFERENCES

- Anttil, F., and M. A. Donelan, 1996: Air–water momentum flux observed over shoaling waves. *J. Phys. Oceanogr.*, **26**, 1344–1353, doi:10.1175/1520-0485(1996)026<1344:AMFOOS>2.0.CO;2.
- Babanin, A. V., and Y. P. Soloviev, 1998: Field investigation of transformation of the wind wave frequency spectrum with fetch and the stage of development. *J. Phys. Oceanogr.*, **28**, 563–576, doi:10.1175/1520-0485(1998)028<0563:FIOTOT>2.0.CO;2.
- Badulin, S. I., A. N. Pushkarev, D. Resio, and V. E. Zakharov, 2005: Self-similarity of wind-driven seas. *Nonlinear Processes Geophys.*, **12**, 891–946, doi:10.5194/npg-12-891-2005.
- , A. V. Babanin, D. Resio, and V. Zakharov, 2007: Weakly turbulent laws of wind–wave growth. *J. Fluid Mech.*, **591**, 339–378, doi:10.1017/S0022112007008282.
- Black, P. G., and Coauthors, 2007: Air–sea exchange in hurricanes: Synthesis of observations from the Coupled Boundary Layer Air–Sea Transfer experiment. *Bull. Amer. Meteor. Soc.*, **88**, 357–374, doi:10.1175/BAMS-88-3-357.
- Burling, R. W., 1959: The spectrum of waves at short fetches. *Disch. Hydrogr. Z.*, **12**, 96–117, doi:10.1007/BF02019818.
- Dean, R. G., and R. A. Dalrymple, 1991: *Water Wave Mechanics for Engineers and Scientist*. World Scientific, 353 pp.
- Dobson, F., W. Perrie, and B. Toulany, 1989: On the deep-water fetch laws for wind-generated surface gravity waves. *Atmos.–Ocean*, **27**, 210–236, doi:10.1080/07055900.1989.9649334.
- Donelan, M. A., 1979: On the fraction of wind momentum retained by waves. *Marine Forecasting*, J. C. J. Nihoul, Ed., Elsevier, 141–159.
- , J. Hamilton, and W. H. Hui, 1985: Directional spectra of wind-generated waves. *Philos. Trans. Roy. Soc. London*, **A315**, 509–562, doi:10.1098/rsta.1985.0054.
- Felizardo, F., and W. K. Melville, 1995: Correlations between ambient noise and the ocean surface wave field. *J. Phys. Oceanogr.*, **25**, 513–532, doi:10.1175/1520-0485(1995)025<0513:CBANAT>2.0.CO;2.
- Gagnaire-Renou, E., M. Benoit, and S. I. Badulin, 2011: On weakly turbulent scaling of wind sea in simulations of fetch-limited growth. *J. Fluid Mech.*, **669**, 178–213, doi:10.1017/S0022112010004921.
- García-Nava, H., F. J. Ocampo-Torres, P. Osuna, and M. A. Donelan, 2009: Wind stress in the presence of swell under moderate to strong wind conditions. *J. Geophys. Res.*, **114**, C12008, doi:10.1029/2009JC005389.
- Hasselmann, K., and Coauthors, 1973: Measurements of wind-wave growth and swell decay during the Joint North Sea Wave Project (JONSWAP). *Ergänzungsheft zur Deutschen Hydrographischen Zeitschrift Reihe A* 12, 93 pp.
- Holthuijsen, L. H., M. D. Powell, and J. D. Pietrzak, 2012: Wind and waves in extreme hurricanes. *J. Geophys. Res.*, **117**, C09003, doi:10.1029/2012JC007983.
- Hwang, P. A., 2004: Influence of wavelength on the parameterization of drag coefficient and surface roughness. *J. Oceanogr.*, **60**, 835–841, doi:10.1007/s10872-005-5776-3.
- , 2005a: Comparison of the ocean surface wind stress computed with different parameterization functions of the drag coefficient. *J. Oceanogr.*, **61**, 91–107, doi:10.1007/s10872-005-0022-6.
- , 2005b: Drag coefficient, dynamic roughness and reference wind speed. *J. Oceanogr.*, **61**, 399–413, doi:10.1007/s10872-005-0050-2.
- , 2006: Duration- and fetch-limited growth functions of wind-generated waves parameterized with three different scaling wind velocities. *J. Geophys. Res.*, **111**, C02005, doi:10.1029/2005JC003180.
- , 2009: Estimating the effective energy transfer velocity at air–sea interface. *J. Geophys. Res.*, **114**, C11011, doi:10.1029/2009JC005497.
- , 2011: A note on the ocean surface roughness spectrum. *J. Atmos. Oceanic Technol.*, **28**, 436–443, doi:10.1175/2010JTECH0812.1.
- , 2016: Fetch- and duration-limited nature of surface wave growth inside tropical cyclones: With applications to air–sea exchange and remote sensing. *J. Phys. Oceanogr.*, **46**, 41–56, doi:10.1175/JPO-D-15-0173.1.
- , and D. W. Wang, 2004: Field measurements of duration limited growth of wind-generated ocean surface waves at young

- stage of development. *J. Phys. Oceanogr.*, **34**, 2316–2326, doi:[10.1175/1520-0485\(2004\)034<2316:FMODGO>2.0.CO;2](https://doi.org/10.1175/1520-0485(2004)034<2316:FMODGO>2.0.CO;2); Corrigendum, **35**, 268–270, doi:[10.1175/JPO-2731.1](https://doi.org/10.1175/JPO-2731.1).
- , and M. A. Sletten, 2008: Energy dissipation of wind-generated waves and whitecap coverage. *J. Geophys. Res.*, **113**, C02012, doi:[10.1029/2007JC004277](https://doi.org/10.1029/2007JC004277); Corrigendum, **114**, C02015, doi:[10.1029/2008JC005244](https://doi.org/10.1029/2008JC005244).
- , H. García-Nava, and F. J. Ocampo-Torres, 2011a: Dimensionally consistent similarity relation of ocean surface friction coefficient in mixed seas. *J. Phys. Oceanogr.*, **41**, 1227–1238, doi:[10.1175/2011JPO4566.1](https://doi.org/10.1175/2011JPO4566.1).
- , —, and —, 2011b: Observations of wind wave development in mixed seas and unsteady wind forcing. *J. Phys. Oceanogr.*, **41**, 2343–2362, doi:[10.1175/JPO-D-11-044.1](https://doi.org/10.1175/JPO-D-11-044.1).
- , D. M. Burrage, D. W. Wang, and J. C. Wesson, 2013: Ocean surface roughness spectrum in high wind condition for microwave backscatter and emission computations. *J. Atmos. Oceanic Technol.*, **30**, 2168–2188, doi:[10.1175/JTECH-D-12-00239.1](https://doi.org/10.1175/JTECH-D-12-00239.1).
- Janssen, J. A. M., 1997: Does wind stress depend on sea-state or not?—A statistical error analysis of HEXMAX data. *Bound.-Layer Meteor.*, **83**, 479–503, doi:[10.1023/A:1000336814021](https://doi.org/10.1023/A:1000336814021).
- Janssen, P., 2004: *The Interaction of Ocean Waves and Wind*. Cambridge University Press, 300 pp.
- Jarosch, E., D. A. Mitchell, D. W. Wang, and W. J. Teague, 2007: Bottom-up determination of air-sea momentum exchange under a major tropical cyclone. *Science*, **315**, 1707–1709, doi:[10.1126/science.1136466](https://doi.org/10.1126/science.1136466).
- Kahma, K. K., and C. J. Calkoen, 1992: Reconciling discrepancies in the observed growth of wind-generated waves. *J. Phys. Oceanogr.*, **22**, 1389–1405, doi:[10.1175/1520-0485\(1992\)022<1389:RDITOG>2.0.CO;2](https://doi.org/10.1175/1520-0485(1992)022<1389:RDITOG>2.0.CO;2).
- , and —, 1994: Growth curve observations. *Dynamics and Modeling of Ocean Waves*, G. J. Komen et al., Eds., Cambridge University Press, 74–182.
- Kim, D.-J., W. M. Moon, S.-E. Park, J.-E. Kim, and H.-S. Lee, 2007: Dependence of waterline mapping on radar frequency used for SAR images in intertidal areas. *IEEE Geosci. Remote Sens. Lett.*, **4**, 269–273, doi:[10.1109/LGRS.2006.888843](https://doi.org/10.1109/LGRS.2006.888843).
- Komen, G. J., L. Cavaleri, M. Donelan, K. Hasselmann, S. Hasselmann, and P. A. E. M. Jessen, Eds., 1994: *Dynamics and Modeling of Ocean Waves*. Cambridge University Press, 532 pp.
- Merzi, N., and W. H. Graf, 1985: Evaluation of the drag coefficient considering the effects of mobility of the roughness elements. *Ann. Geophys.*, **3**, 473–478.
- Moon, I.-J., I. Ginis, T. Hara, H. L. Tolman, C. W. Wright, and E. J. Walsh, 2003: Numerical simulation of sea surface directional wave spectra under hurricane wind forcing. *J. Phys. Oceanogr.*, **33**, 1680–1706, doi:[10.1175/2410.1](https://doi.org/10.1175/2410.1).
- Ocampo-Torres, F. J., H. García-Nava, R. Durazo, P. Osuna, G. M. Díaz Méndez, and H. C. Graber, 2011: The INTOA experiment: A study of ocean-atmosphere interactions under moderate to strong offshore winds and opposing swell conditions, in the Gulf of Tehuantepec, Mexico. *Bound.-Layer Meteor.*, **138**, 433–451, doi:[10.1007/s10546-010-9561-5](https://doi.org/10.1007/s10546-010-9561-5).
- Phillips, O. M., 1985: Spectral and statistical properties of the equilibrium range in wind-generated gravity waves. *J. Fluid Mech.*, **156**, 505–531, doi:[10.1017/S0022112085002221](https://doi.org/10.1017/S0022112085002221).
- Pierson, W. J., and L. Moskowitz, 1964: A proposed spectral form for full, developed wind seas based on the similarity theory of S. A. Kitaigorodskii. *J. Geophys. Res.*, **69**, 5181–5190, doi:[10.1029/JZ069i024p05181](https://doi.org/10.1029/JZ069i024p05181).
- Plant, W. J., 1982: A relationship between wind stress and wave slope. *J. Geophys. Res.*, **87**, 1961–1967, doi:[10.1029/JC087iC03p01961](https://doi.org/10.1029/JC087iC03p01961).
- Powell, M. D., 2006: Drag coefficient distribution and wind speed dependence in tropical cyclones. Final Rep. to the NOAA JHT Program, 26 pp.
- , P. J. Vickery, and T. A. Reinhold, 2003: Reduced drag coefficient for high wind speeds in tropical cyclones. *Nature*, **422**, 279–283, doi:[10.1038/nature01481](https://doi.org/10.1038/nature01481).
- Romero, L., and W. K. Melville, 2010: Airborne observations of fetch-limited waves in the Gulf of Tehuantepec. *J. Phys. Oceanogr.*, **40**, 441–465, doi:[10.1175/2009JPO4127.1](https://doi.org/10.1175/2009JPO4127.1).
- Sletten, M. A., and P. A. Hwang, 2011: The effect of wind-wave growth on SAR-based waterline maps. *IEEE Trans. Geosci. Remote Sens.*, **49**, 5140–5149, doi:[10.1109/TGRS.2011.2154362](https://doi.org/10.1109/TGRS.2011.2154362).
- Sverdrup, H. U., and W. H. Munk, 1947: Wind, sea, and swell: Theory of relations for forecasting. U. S. Navy Hydrographic Office Tech. Rep. 1, 60 pp.
- Terray, E. A., M. A. Donelan, Y. C. Agrawal, W. M. Drennan, K. K. Kahma, A. J. Williams, P. A. Hwang, and S. A. Kitaigorodskii, 1996: Estimates of kinetic energy dissipation under breaking waves. *J. Phys. Oceanogr.*, **26**, 792–807, doi:[10.1175/1520-0485\(1996\)026<0792:EOKEDU>2.0.CO;2](https://doi.org/10.1175/1520-0485(1996)026<0792:EOKEDU>2.0.CO;2).
- Walsh, E. J., D. W. Hancock, D. E. Hines, R. N. Swift, and J. F. Scott, 1985: Directional wave spectra measured with the surface contour radar. *J. Phys. Oceanogr.*, **15**, 566–592, doi:[10.1175/1520-0485\(1985\)015<0566:DWSMWT>2.0.CO;2](https://doi.org/10.1175/1520-0485(1985)015<0566:DWSMWT>2.0.CO;2).
- , —, —, —, and —, 1989: An observation of the directional wave spectrum evolution from shoreline to fully developed. *J. Phys. Oceanogr.*, **19**, 670–690, doi:[10.1175/1520-0485\(1989\)019<0670:A0OTDW>2.0.CO;2](https://doi.org/10.1175/1520-0485(1989)019<0670:A0OTDW>2.0.CO;2).
- Wright, C. W., and Coauthors, 2001: Hurricane directional wave spectrum spatial variation in the open ocean. *J. Phys. Oceanogr.*, **31**, 2472–2488, doi:[10.1175/1520-0485\(2001\)031<2472:HDWSSV>2.0.CO;2](https://doi.org/10.1175/1520-0485(2001)031<2472:HDWSSV>2.0.CO;2).
- Young, I. R., 1988: Parametric hurricane wave prediction model. *J. Waterw. Port Coastal Ocean Eng.*, **114**, 637–652, doi:[10.1061/\(ASCE\)0733-950X\(1988\)114:5\(637\)](https://doi.org/10.1061/(ASCE)0733-950X(1988)114:5(637)).
- , 1998: Observations of the spectra of hurricane generated waves. *Ocean Eng.*, **25**, 261–276, doi:[10.1016/S0029-8018\(97\)00011-5](https://doi.org/10.1016/S0029-8018(97)00011-5).
- , 1999: *Wind Generated Ocean Waves*. Elsevier, 288 pp.
- , 2003: A review of the sea state generated by hurricanes. *Mar. Struct.*, **16**, 201–218, doi:[10.1016/S0951-8339\(02\)00054-0](https://doi.org/10.1016/S0951-8339(02)00054-0).
- , 2006: Directional spectra of hurricane wind waves. *J. Geophys. Res.*, **111**, C08020, doi:[10.1029/2006JC003540](https://doi.org/10.1029/2006JC003540).
- , and G. Ph. van Vledder, 1993: A review of the central role of nonlinear interactions in wind-wave evolution. *Philos. Trans. Roy. Soc. London*, **A342**, 505–524, doi:[10.1098/rsta.1993.0030](https://doi.org/10.1098/rsta.1993.0030).
- , and J. Vinoth, 2013: An “extended fetch” model for the spatial distribution of tropical cyclone wind-waves as observed by altimeter. *Ocean Eng.*, **70**, 14–24, doi:[10.1016/j.oceaneng.2013.05.015](https://doi.org/10.1016/j.oceaneng.2013.05.015).
- Zakharov, V. E., 2005: Theoretical interpretation of fetch limited wind-driven sea observations. *Nonlinear Processes Geophys.*, **12**, 1011–1020, doi:[10.5194/npg-12-1011-2005](https://doi.org/10.5194/npg-12-1011-2005).
- , S. I. Badulin, P. A. Hwang, and G. Caulliez, 2015: Universality of sea wave growth and its physical roots. *J. Fluid Mech.*, **780**, 503–535, doi:[10.1017/jfm.2015.468](https://doi.org/10.1017/jfm.2015.468).